Optimization of Quasi-Halbach Topologies to Maximize the Acceleration of Moving-Magnet Planar Motors

M. Kleijer, J. W. Jansen and E. A. Lomonova

***Abstract*—This paper concerns the optimization of eight different quasi-Halbach magnet array structures that are used in a dual-layer moving-magnet planar motor. These magnet arrays vary in number of magnets per pole and contain both cuboidal and trapezoidal prism magnet shapes. The parameters of the magnet structures are optimized to maximize the acceleration of the planar motor. The resulting accelerations and force ripples of the planar motor are compared for the optimal magnet structures. The results show that the studied magnet arrays improve the acceleration of the planar motor compared to the benchmark magnet array with three cuboidal magnets per pole. A maximum increase in acceleration of 10.1 % is achieved, while the force ripple is reduced by 10.2 % in any direction of movement.**

***Index Terms*—Planar motor, Magnetic levitation, Permanent magnets, Optimization**

I. Introduction

The semiconductor industry requires higher accelerations and position tracking accuracies from wafer positioning systems to improve the throughput of e.g. lithography equipment. Magnetically levitated coreless planar motors are applied in these positioning systems to provide movement in six degrees-of-freedom. Two types of planar motor topologies exist: moving-coil configurations [1], [2] and moving-magnet arrangements [3]–[7]. The benefit of the moving-magnet planar motor is the relatively low moving mass, since connections to the moving part, in the form of power cables and cooling hoses, are not required. However, in these motors the mass of the magnets is a significant part of the total moving mass. Contrary to the moving-coil planar motors, the acceleration of these motors cannot be improved by increasing the magnetic loading in the form of adding magnetic material, as this will also increase the levitated moving mass.

The moving-magnet planar motors of [3]–[7] use quasi-Halbach magnet array structures. Such a magnet array approximates an ideal sinusoidal magnetization pattern, which provides a flux focusing effect [8]. This results in a higher magnetic loading compared to a magnet array that has alternating poles in a single direction [9]. In [3]–[5] quasi-Halbach topologies with three magnets per pole (MPP) are used. In [6] a quasi-Halbach magnet array is introduced that consist of seven MPP and this topology is compared with the magnet array of [3]. The results show a higher magnetic loading when seven MPP are used. The quasi-Halbach topologies described in [3]–[6] are constructed with cuboidal magnets. In [7], [10] various quasi-Halbach magnet arrays are described that use trapezoidal prism magnet shapes and these topologies are compared with the magnet array of [3]. The magnet arrays with trapezoidal magnets show a higher magnetic loading.

Besides the effect on the magnetic loading the higher number of MPP and the application of the trapezoidal prism magnets also influences the higher harmonic components of the magnetic flux density distribution. The quasi-Halbach magnet arrays introduced in [6], [10] show a reduction in the higher harmonic content of the magnetic flux density distribution compared to the magnet array of [3].

In this paper, a study is conducted to verify the effect of quasi-Halbach magnet arrays with multiple MPP and trapezoidal prism magnets on the acceleration and the force ripple of a dual-layer moving-magnet planar motor. Eight magnet structures are introduced that have a different number of MPP and consist of both cuboidal and trapezoidal prism magnets. A semi-analytical modeling framework that is based on magnetic charge modeling is used for the modeling of the planar motor. The magnet dimensions and the magnetization angles in the various magnet structures are optimized with a parametric search to maximize the fundamental component of the magnetic flux density distribution in the airgap per unit mass. A comparison of the resulting acceleration and force ripple is made between the optimal topologies.

II. Moving-magnet planar motor topology

A segment of the dual-layer moving-magnet planar motor that is studied to investigate the effect of the various magnet structures on the motor performance in terms of acceleration and force ripple is shown in Fig. 1. It consists of a stator with six coreless coils in two layers and a translator with a magnet array glued to a support structure. The magnet topology that consists of three cuboidal MPP is shown as an example. The size of the translator spans 25 magnet poles. The combined mass of the support structure and the corresponding payload of this segment is assumed to be, $m_{support}$. The translator has a local coordinate frame

$$\vec{x}_m = [x_m \;\; y_m \;\; z_m]^\top, \tag{1}$$

that is rotated by 45° with respect to the global coordinate frame of the stator

$$\vec{x}_c = [x_c \;\; y_c \;\; z_c]^\top. \tag{2}$$

The authors are with the Department of Electrical Engineering, Eindhoven University of Technology, 5612 AZ Eindhoven, The Netherlands (e-mail: m.kleijer@tue.nl).

The stator coils are placed in two layers [4], oriented in the, x_c-, and y_c-directions, with a three-phase arrangement. To ensure that the force of each coil is decoupled (the top coil layer is capable of producing force in the, x_c-, and z_c-directions, whereas the bottom coil layer is capable of producing force in the, y_c-, and z_c-directions) the length of a coil, l_c, equals an even times the pole pitch of the magnet array, τ_n. In this segment the coil length is, $2\tau_n$.

The harmonic amplitudes of the magnetic flux density distribution of the magnet array decay with [11]

$$e^{\frac{-\pi\vec{p}}{\tau}\sqrt{k^2+l^2}}, \tag{3}$$

where, k, and, l, are the harmonic numbers in the, x_m-, and y_m-directions, respectively, and, $\vec{p}$, is the position of the magnet array with respect to the global coordinate frame

$$\vec{p} = [p_x \;\; p_y \;\; p_z]^\top. \tag{4}$$

The top coil layer is closer to the magnet plate compared to the bottom layer and will produce a higher force per unit of dissipated power in case the coil heights, h_c, are equal. Therefore, the coil heights are optimized such that the bottom coil layer equals the top layer in terms of dissipated power required for levitation of the translator [4]. The other coil dimensions are optimized to minimize this power dissipation. The corresponding parameters are specified in Table I.

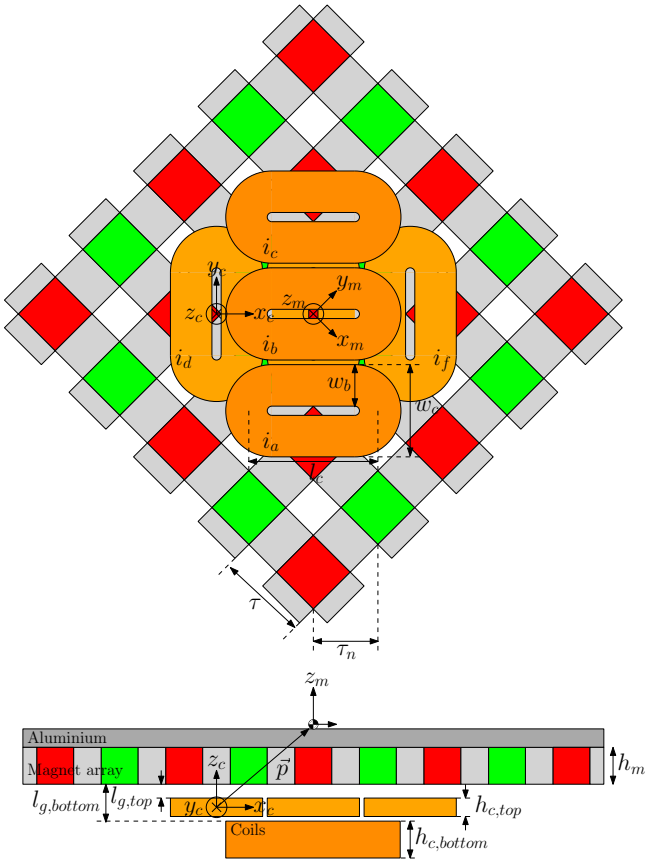

Fig. 1. Bottom view and cross-sectional view of the moving-magnet planar motor segment.

TABLE I
PARAMETERS OF THE PLANAR MOTOR SEGMENT.

Parameter	Symbol	Value	Unit
Magnet pitch	τ	33.3	mm
Magnet pitch ($\tau/\sqrt{2}$)	τ_n	23.5	mm
Magnet height	h_m	8.0	mm
Magnet mass density	ρ_m	7700	kg/m^3
Remanent flux density	B_r	1.28	T
Coil length	l_c	47.1	mm
Coil width	w_c	31.4	mm
Coil bundle width	w_b	14.6	mm
Top coil height	$h_{c,top}$	2.1	mm
Bottom coil height	$h_{c,bottom}$	7.8	mm
Current density	J	10.0	A/mm^2
Top airgap length	$l_{g,top}$	1.4	mm
Bottom airgap length	$l_{g,bottom}$	4.9	mm
Support mass	$m_{support}$	1.0	kg
Epoxy mass density	ρ_e	1500	kg/m^3

III. MODELING OF THE PLANAR MOTOR

For analysis of the planar motor segment a semi-analytical model is used [1], [11]. The magnet array is modeled using magnetic charge modeling and the force is calculated with the Lorentz force. The torque acting on the magnet array is neglected.

The analytical solution of the magnetic flux density for a cuboidal magnet is provided in [12]. A similar magnetic flux density solution for a triangular prism shaped magnet is described in [13]. These solutions assume that the relative permeability equals unity in- and out-side the permanent magnet. The error due to this assumption is small, since high quality sintered NdFeB permanent magnets are used in the planar motor. By combining the magnetic flux density calculations of these two magnet shapes a trapezoidal prism magnet can be realized that is composed of a single cuboidal magnet with a triangular magnet on both sides, as is shown in Fig. 2. Using translations, rotations and superposition, the magnetic flux density distributions of the magnet plate structures of Section IV can be evaluated.

Since the stator coils are coreless the force on the magnet array by a single coil can be obtained by the Lorentz force

$$\vec{F}(\vec{p}) = -\int_{V_{\text{coil}}} \vec{J}(\vec{x}_c) \times \vec{B}(\vec{x}_c - \vec{p})\mathrm{d}V, \tag{5}$$

where, V_{coil}, is the coil volume, $\vec{J}$, is the current density in the coil and, $\vec{B}$, is the magnetic flux density solution of the magnet array. The integral of (5) is evaluated numerically with the trapezoidal rule using a cuboidal mesh with a discretization of 2.0 mm.

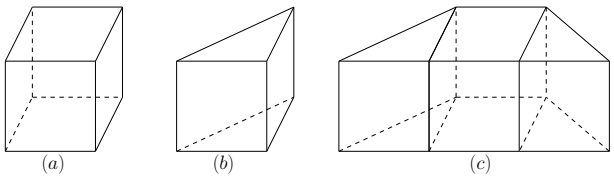

Fig. 2. Magnet shapes used in the modeling framework: (*a*) cuboidal magnet, (*b*) triangular prism magnet and (*c*) trapezoidal prism magnet, which comprises of a single cuboidal magnet with a triangular magnet on both sides.

The force produced by the bottom coil set is expressed as

$$\vec{F}_{bottom} = \begin{bmatrix} F_{y,bottom} \\ F_{z,bottom} \end{bmatrix} = \Gamma_{\mathbf{F},bottom}(\vec{p})^{\top} \begin{bmatrix} i_a \\ i_b \\ i_c \end{bmatrix}, \quad (6)$$

where, i_a, i_b, and, i_c, are the three-phase currents of the bottom coil. The matrix, $\Gamma_{\mathbf{F},bottom}(\vec{p})$, is defined as

$$\begin{bmatrix} -K_y(p_z)\sin\left(\frac{\pi p_x}{\tau_n}\right) & -K_z(p_z)\cos\left(\frac{\pi p_x}{\tau_n}\right) \\ -K_y(p_z)\sin\left(\frac{\pi p_x}{\tau_n}+\frac{4\pi}{3}\right) & -K_z(p_z)\cos\left(\frac{\pi p_x}{\tau_n}+\frac{4\pi}{3}\right) \\ -K_y(p_z)\sin\left(\frac{\pi p_x}{\tau_n}-\frac{4\pi}{3}\right) & -K_z(p_z)\cos\left(\frac{\pi p_x}{\tau_n}-\frac{4\pi}{3}\right) \end{bmatrix}, \quad (7)$$

where, $K_y(p_z)$, and, $K_z(p_z)$, are the force functions in the, y_c-, and z_c-directions, which are obtained by evaluating the Lorentz force over the individual coils for a constant current density. To limit the computational effort the Lorentz force is only evaluated for the middle coil. The centre of the magnet array is moved in a plane from $-\tau_n$ to τ_n in the, x_c-, and y_c-directions with respect to the coil layers. This plane is shown by the blue square in Fig. 3. The first extreme translator position at (-τ_n, -τ_n) is highlighted by the solid black line. The other three extreme translator positions are shown with the dotted red lines. Due to the sizing of the magnet array the end-effects are removed and no even harmonics occur. The resulting force function of a single coil with a constant current density is interpolated to account for the spatial phase shift of the other coils in the layer. Superposition is applied to obtain the total force function of the bottom coil set. The same approach is used for the top coil layer. The three-phase coil sets are excited such that the bottom coil layer produces equal and constant force in the, y_c-, and z_c-directions and the top coil layer produces equal and constant force in the, x_c-, and z_c-directions. With the commutated forces the force ripples of the magnet plate structures of Section IV are evaluated.

IV. Magnet Topologies

The eight investigated magnet topologies are shown in Fig. 4 to Fig. 11. For each topology a periodic segment with two poles is shown. The cross-sectional view of the topologies shows the magnet arrangement in the $x_m z_m$-plane,

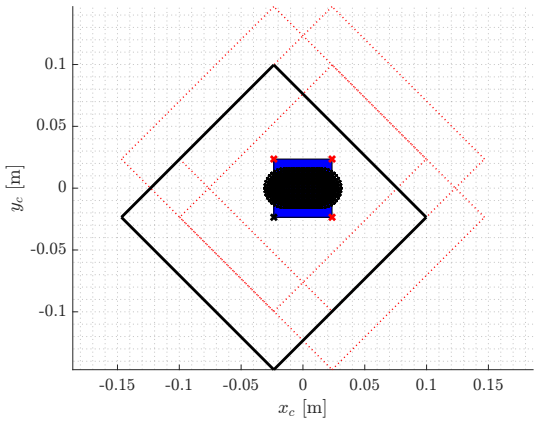

Fig. 3. Translator centre positions to analyze the force distribution on the magnet structure produced by the middle coil of the bottom coil layer.

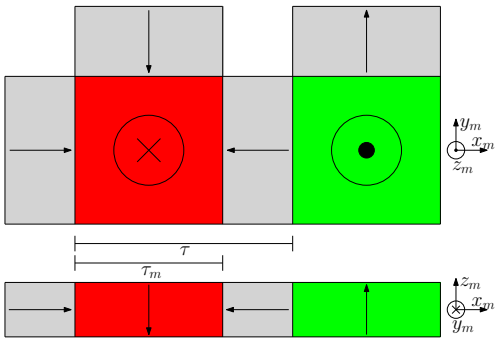

Fig. 4. Top view and cross-sectional view of a segment of the cuboidal 3-MPP magnet topology.

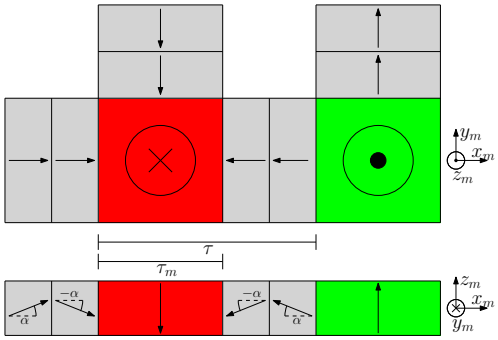

Fig. 5. Top view and cross-sectional view of a segment of the cuboidal 5-MPP magnet topology.

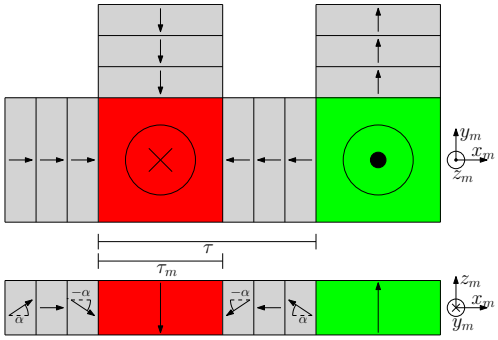

Fig. 6. Top view and cross-sectional view of a segment of the cuboidal 7-MPP magnet topology.

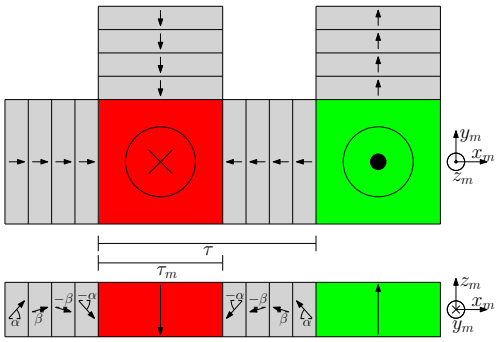

Fig. 7. Top view and cross-sectional view of a segment of the cuboidal 9-MPP magnet topology.

which has symmetry with the $y_m z_m$-plane. The dimensions of the magnets are determined by the value of the ratio, $\frac{\tau_m}{\tau}$, where, τ_m, is the size of the magnet magnetized in the z_m-direction. The ratio in the figures is in accordance with the optimization results, which are elaborated in Section V. The topology of Fig. 4 consists of cuboidal magnets and a single pole consists of three magnets. This cuboidal 3-MPP topology is considered as benchmark, since it is applied in [3]–[5]. By replacing the cuboidal magnets, magnetized in the, x_m-, and y_m-directions, with trapezoidal prism magnets the available volume of a single pole is filled with magnet material, which improves the magnetic loading. The resulting trapezoidal 3-MPP topology is shown in Fig. 8. The remaining structures have increasing MPP, which improves the approximation of the ideal sinusoidal magnetization pattern. The topologies with cuboidal magnets and higher number of MPP are shown in Fig. 5 to Fig. 7. Multiple magnets that are magnetized in the, x_m-, and y_m-directions are positioned between the two magnets magnetized in the z_m-direction. These magnets have equal dimensions and magnetization angles, α, and, β. The topologies with trapezoidal magnets and higher number of MPP are shown in Fig. 9 to Fig. 11.

V. Optimization of the Magnet Topologies

For each of the magnet topologies the magnetic flux density distribution is calculated, from which the harmonic content, $B_{(k,l)}$, is extracted by Fourier decomposition. The optimization objective of the parametric search is to maximize the fundamental component of the magnetic flux density distribution per unit of mass, $\frac{B_{(1,1)}}{m}$, in the middle of the airgap, $\frac{1}{2}l_{g,top}$. This relates directly to the acceleration of the planar motor. The optimization variables are the ratio, $\frac{\tau_m}{\tau}$, and the angles, α, and, β. The pole pitch and the magnet height, h_m, are fixed. The ratio, $\frac{\tau_m}{\tau}$, ranges from 0.05 to 0.95 and, where applicable, the angles range from 5.0° to 85.0°.

The mass of the four topologies with the trapezoidal prism magnets is equal for every ratio, $\frac{\tau_m}{\tau}$, since the available volume for a single pole of these topologies is filled with magnet material. The total moving mass of the segment equals 2.71 kg for the trapezoidal topologies. For the cuboidal topologies empty spaces are present in the volume of a single pole. These empty spaces are assumed to be filled with an epoxy resin. The ratio, $\frac{\tau_m}{\tau}$, determines the ratio of magnet volume and volume of the epoxy-filled spaces. Since the mass density of epoxy, ρ_e, is lower compared to the mass density of the magnets, ρ_m, the mass of the cuboidal topologies changes accordingly. The moving mass for the cuboidal topologies ranges from 1.47 kg for a ratio of 0.05 to a mass of 2.70 kg for a ratio of 0.95.

Figure 12 shows the results of the parametric search. Table II compares these optimization results. The comparison shows that, except for the trapezoidal 3-MPP topology, all topologies reach higher acceleration compared to the benchmark. For the topologies with cuboidal magnets two aspects contribute to the higher acceleration. First, the cuboidal topologies with a higher number of MPP have a lower mass compared to the 3-MPP topology. The mass is 2.76 %

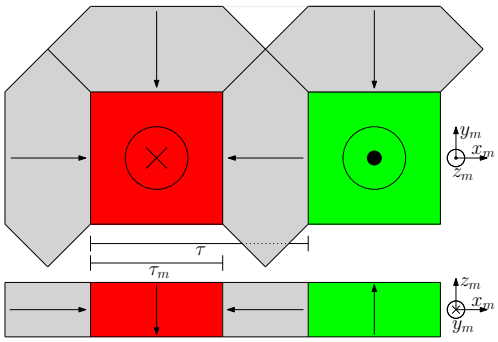

Fig. 8. Top view and cross-sectional view of a segment of the trapezoidal 3-MPP magnet topology.

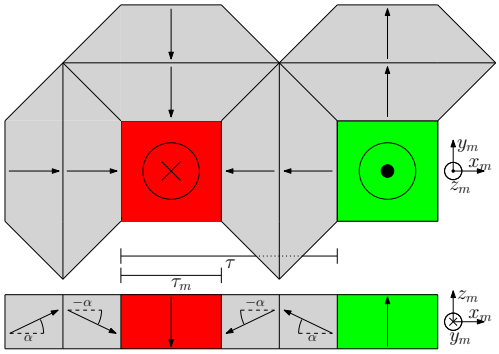

Fig. 9. Top view and cross-sectional view of a segment of the trapezoidal 5-MPP magnet topology.

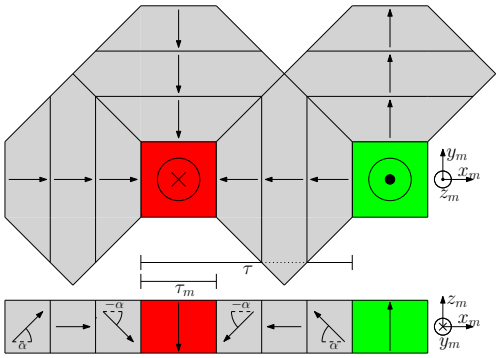

Fig. 10. Top view and cross-sectional view of a segment of the trapezoidal 7-MPP magnet topology.

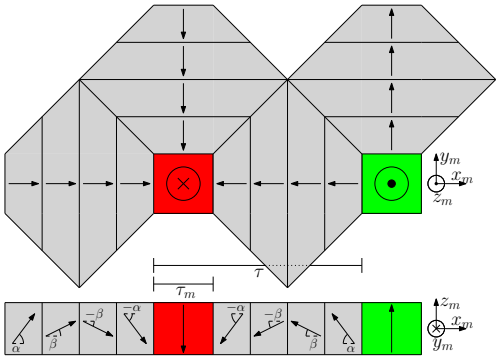

Fig. 11. Top view and cross-sectional view of a segment of the trapezoidal 9-MPP magnet topology.

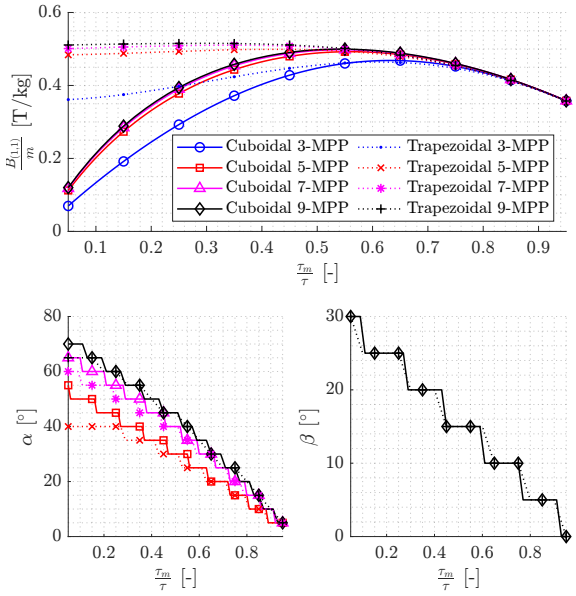

Fig. 12. Fundamental component of the magnetic flux density distribution in the airgap per unit mass of the different magnet structures for varying ratio (top figure) and the corresponding optimal values of the angles for each value of the ratio (bottom figures).

lower for the 5-MPP topology and 3.54 % lower for both the 7-MPP and 9-MPP topologies. Second, the fundamental component of the magnetic flux density distribution in the airgap is increasingly higher for the topologies with more MPP compared to the benchmark. The maximum acceleration improvement equals 6.65 % for the 9-MPP topology. For the topologies with trapezoidal magnets the mass is 6.23 % higher compared to the cuboidal 3-MPP topology. However, the acceleration increases for the topologies with 5-MPP or higher compared to the benchmark due to the higher magnetic loading. The maximum acceleration improvement equals 10.1 % for the 9-MPP topology, which shows the benefit of the trapezoidal prism magnets and the higher number of MPP combined. Figure 12 shows that all eight topologies have equal acceleration for ratios, $\frac{\tau_m}{\tau}$, higher than 0.75. For these ratios the magnets magnetized in the z_m-direction become dominant in size, which nullifies the effect of the other magnets on the magnetic flux density distribution. When the magnets magnetized in the z_m-direction become smaller in size the angles of the magnets magnetized in the, x_m-, and y_m-directions increase. This effect is more apparent when the number of MPP is higher. This behavior is similar for the cuboidal and trapezoidal magnet topologies. Finally, for the trapezoidal topologies with 5-MPP, 7-MPP and 9-MPP the maximum acceleration varies less than 1.00 % for ratios between 0.05 and 0.45. This could provide additional freedom in the design of these magnet structures.

VI. Force Ripple

The harmonic content of the magnetic flux density and the corresponding force distribution is evaluated for each coil layer with the magnet array parameters described in Table II. Fourier decomposition is applied to the resulting distributions

TABLE II
Comparison of the optimization results to maximize the fundamental magnetic flux density component in the middle of the airgap of the magnet topologies.

Topology	α [°]	β [°]	$\frac{\tau_m}{\tau}$ [-]	m [kg]	$\frac{B_{(1,1)}}{m}$ [T/kg]	$\Delta\frac{B_{(1,1)}}{m}$ [%]
Cuboidal 3-MPP	-	-	0.65	2.54	0.47	-
Cuboidal 5-MPP	25	-	0.58	2.47	0.49	5.12
Cuboidal 7-MPP	35	-	0.57	2.45	0.50	6.26
Cuboidal 9-MPP	40	15	0.57	2.45	0.50	6.65
Trapezoidal 3-MPP	-	-	0.61	2.71	0.46	-0.90
Trapezoidal 5-MPP	35	-	0.45	2.71	0.50	6.52
Trapezoidal 7-MPP	45	-	0.37	2.71	0.51	8.91
Trapezoidal 9-MPP	55	20	0.30	2.71	0.52	10.1

and the first six higher harmonics with the most significant amplitude values are extracted. The harmonic spectrums of the magnetic flux density distribution are evaluated in the middle of the individual coil layers. The resulting spectrums of the magnetic flux density in the z_m-direction are shown in Fig. 13. The harmonic spectrum is equal for all directions. Therefore, the harmonic spectrums of the magnetic flux density distributions in the, x_m-, and y_m-directions are not shown separately. The harmonics marked with an asterisk also contain their dual: (3,1)* means (3,1), (1,3). The shape of the harmonic content of the magnetic flux density is similar for both coil layers. However, the amplitudes decay in the z_c-direction according to (3). Consequently, the harmonic amplitudes are lower for the bottom coil layer compared to the top coil layer. The (3,1), (1,3) and (3,3) harmonics are the most dominant. Furthermore, the spectrums show that the trapezoidal topologies have higher amplitudes for the (3,3) and (5,5) harmonics, compared to the cuboidal topologies, which originate from the triangular corners of the trapezoidal prism magnets that fill the empty spaces in the magnet array. Compared to the topologies with 3-MPP the structures with a higher number of MPP have lower amplitudes for the (5,1), (1,5), (7,1) and (1,7) harmonics. This shows that these topologies approach the sinusoidal magnetization pattern more closely.

The harmonic spectrums of the commutated forces in all directions for the top coil and bottom coil are shown in Fig 14 and Fig. 15, respectively. The spectrums show that there is a clear relation between the fundamental magnetic flux density component and the DC terms of the forces, but this is not the case for the higher harmonic content. Most of the higher harmonic content present in the magnetic flux density is removed by the commutation, since the forces only contain either the (3,1) and (3,3) harmonics or the (1,3) and (3,3) harmonics. The force spectrums show that the application of the trapezoidal prism magnets or the use of multiple MPP does not influence the force decoupling, since the amplitudes of the decoupled forces, $F_{y,top}$, for the top coil and, $F_{x,bottom}$, for the bottom coil, are less than 0.97 % of the magnitude of the DC-terms of the propulsion forces, $F_{x,top}$, and, $F_{y,bottom}$, and the levitation forces, $F_{z,top}$, and, $F_{z,bottom}$, produced by the top coil and bottom coil, respectively.

The total harmonic distortion (THD) in the magnetic flux density distribution, as well as in the propulsion and levitation

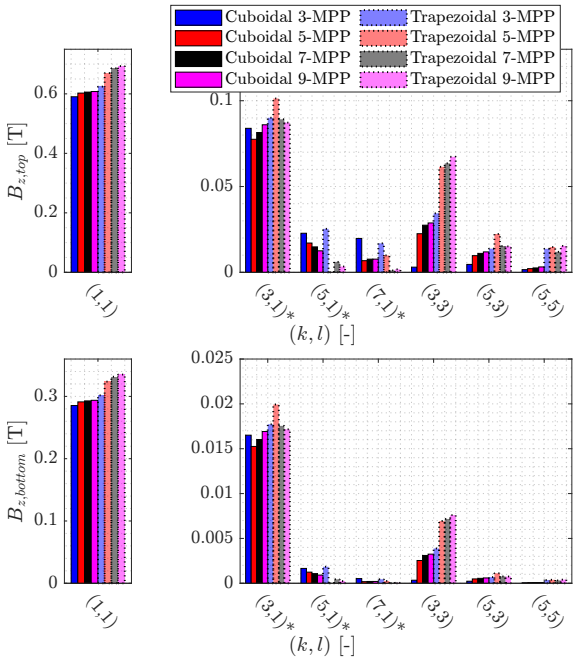

Fig. 13. Harmonic spectrums of the magnetic flux density distribution in the middle of the top coil layer (top figure) and in the middle of the bottom coil layer (bottom figure) for each magnet topology.

forces, is calculated for each of the magnet topologies from the aforementioned spectrums. The THD values are compared to the results of the benchmark topology. Table III shows this comparison for the top coil layer and Table IV for the bottom coil layer. The results show that when the THD in the magnetic flux density decreases for the top coil the THD also decreases in the bottom coil. However, the magnitudes are different, which is caused by the decay of the harmonic content according to (3). Similar results are shown for the THD comparison of both the propulsion and levitation forces between the two coil layers. The magnitudes vary due to the different coil heights. For both the top coil and the bottom coil it is shown that when the THD of the magnetic flux density decreases the THD of the forces also decrease for the same coil. However, the magnitudes do not coincide. The THD in the commutated forces is used for the force ripple comparison of the various magnet topologies, as this quantity contains the most details of the planar motor topology.

The cuboidal topologies with multiple MPP have a lower force ripple compared to the benchmark for both the propulsion and levitation forces. For the trapezoidal 3-MPP and 5-MPP topologies the force ripples are higher, but the force ripple is lower for the trapezoidal 7-MPP and 9-MPP topologies compared to the cuboidal 3-MPP topology. The trapezoidal 9-MPP topology has the highest force ripple reduction with

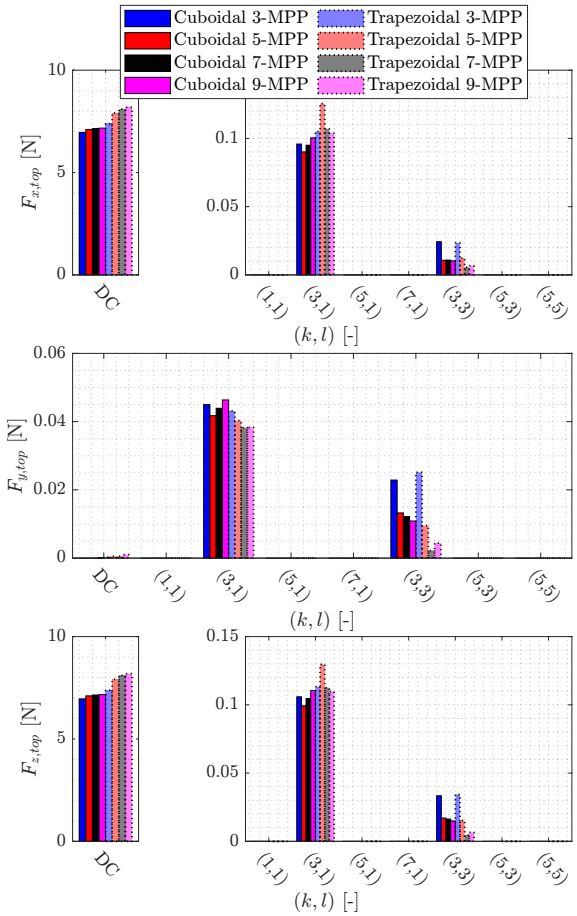

Fig. 14. Harmonic spectrums of the force distributions of the commutated top coil layer for each magnet topology.

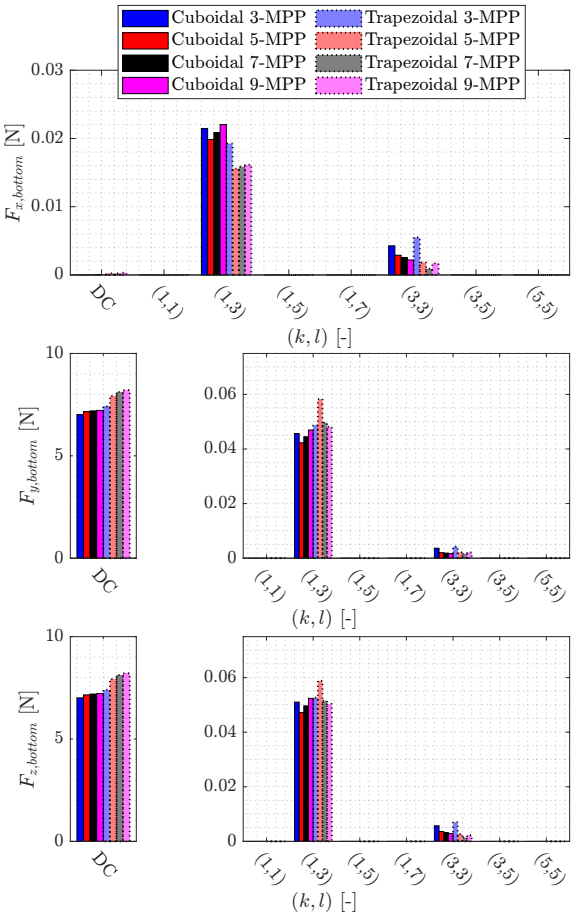

Fig. 15. Harmonic spectrums of the force distributions of the commutated bottom coil layer for each magnet topology.

TABLE III
COMPARISON OF THE THD IN THE FLUX DENSITY AND FORCE DISTRIBUTIONS EVALUATED FOR THE TOP COIL LAYER FOR EACH OF THE MAGNET TOPOLOGIES OPTIMIZED FOR MAXIMUM ACCELERATION.

Topology	Δ THD $B_{z,top}$ [%]	Δ THD $F_{x,top}$ [%]	Δ THD $F_{z,top}$ [%]
Cuboidal 3-MPP	-	-	-
Cuboidal 5-MPP	-10.5	-10.1	-11.1
Cuboidal 7-MPP	-6.37	-5.80	-7.06
Cuboidal 9-MPP	-2.08	-0.94	-2.44
Trapezoidal 3-MPP	4.98	2.68	0.53
Trapezoidal 5-MPP	10.9	12.2	3.47
Trapezoidal 7-MPP	-2.65	-6.83	-12.8
Trapezoidal 9-MPP	-4.03	-10.6	-15.8

TABLE IV
COMPARISON OF THE THD IN THE FLUX DENSITY AND FORCE DISTRIBUTIONS EVALUATED FOR THE BOTTOM COIL LAYER FOR EACH OF THE MAGNET TOPOLOGIES OPTIMIZED FOR MAXIMUM ACCELERATION.

Topology	Δ THD $B_{z,bottom}$ [%]	Δ THD $F_{y,bottom}$ [%]	Δ THD $F_{z,bottom}$ [%]
Cuboidal 3-MPP	-	-	-
Cuboidal 5-MPP	-9.05	-9.44	-9.60
Cuboidal 7-MPP	-4.82	-5.28	-5.59
Cuboidal 9-MPP	-0.04	-0.37	-0.74
Trapezoidal 3-MPP	2.75	1.06	2.08
Trapezoidal 5-MPP	9.04	12.6	1.42
Trapezoidal 7-MPP	-5.27	-6.44	-13.4
Trapezoidal 9-MPP	-7.72	-10.2	-16.2

values of 10.6 %, 10.2 % and 16.2 % in the, x_c, y_c, and, z_c-directions, respectively.

VII. CONCLUSIONS

Eight quasi-Halbach magnet topologies, which vary in number of magnets per pole (MPP) and contain both cuboidal and trapezoidal prism magnets, have been investigated for a dual-layer moving-magnet planar motor application. These topologies are optimized to maximize the fundamental component of the magnetic flux density distribution in the airgap per unit of mass. It is shown that these topologies improve the acceleration of the planar motor compared to the benchmark topology with three cuboidal MPP. Furthermore, it is shown that the total harmonic distortion (THD) of the magnetic flux density distribution does not coincide with the THD of the commutated forces. The comparison of the harmonic content of the commutated forces show that, apart from the trapezoidal 3-MPP and the trapezoidal 5-MPP topologies, the force ripple is lower compared to the benchmark, alongside the higher acceleration. The maximum acceleration improvement compared to the benchmark is equal to 10.1 % for the trapezoidal 9-MPP topology, while the THD of the propulsion force is reduced by 10.2 % and the THD of the levitation force is reduced by 16.2 %.

REFERENCES

[1] J.C. Compter, "Electro-dynamic planar motor", *Precision Engineering*, vol. 28, no. 2, pp. 171-180, 2004.

[2] L. Zhang, B. Kou, F. Xing, et al., "Modeling and analysis of a magnetically levitated synchronous permanent magnet planar motor with concentric structure winding," Proceedings of the 2014 17th International Symposium on Electromagnetic Launch Technology (EML), La Jolla, USA, October 2014, pp. 1-6.

[3] J. W. Jansen, C. M. M. van Lierop, E. A. Lomonova, et al., "Ironless magnetically levitated planar actuator," *Journal of Applied Physics*, vol. 103, no. 7, pp. 1-3, 2008.

[4] J. M. M. Rovers, J. W. Jansen and E. A. Lomonova, "Design and measurements of the double layer planar motor," Proceedings of the 2013 IEEE International Electric Machines & Drives Conference (IEMDC), Chicago, USA, July 2013, pp. 204-211.

[5] C. H. H. M. Custers, I. Proimadis, J. W. Jansen, et al., "Active compensation of the deformation of a magnetically levitated mover of a planar motor," Proceedings of the 2019 IEEE International Electric Machines & Drives Conference (IEMDC), San Diego, USA, August 2019, pp. 854-861.

[6] W. Min, M. Zhang, Y. Zhu, et al., "Analysis and optimization of a new 2-D magnet array for planar motor," *IEEE Transactions on Magnetics*, vol. 46, no. 5, pp. 1167-1171, 2010.

[7] J. Peng and Y. Zhou, "Modeling and analysis of a new 2-d halbach array for magnetically levitated planar motor," *IEEE Transactions on Magnetics*, vol. 49, no. 1, pp. 618–627, 2013.

[8] K. Halbach, "Design of permanent multipole magnets with oriented rare earth cobalt material," *Nuclear Instruments and Methods*, vol. 169, no. 1, pp. 1-10, 1980.

[9] H.-S. Cho, C.-H. Im and H.-K. Jung, "Magnetic field analysis of 2-D permanent magnet array for planar motor," *IEEE Transactions on Magnetics*, vol. 37, no. 5, pp. 3762-3766, 2001.

[10] L. Zhang and B. Kou, "Investigation of a novel 2-D Halbach magnet array for magnetically levitated planar motor," Proceedings of the 2017 20th International Conference on Electrical Machines and Systems (ICEMS), Sydney, Australia, August 2017, pp. 1-5.

[11] J. W. Jansen, C. M. M. van Lierop, E. A. Lomonova, et al., "Modeling of magnetically levitated planar actuators with moving magnets," *IEEE Transactions on Magnetics*, vol. 43, pp. 15–25, 2007.

[12] G. Akoun and J.-P. Yonnet, "3D analytical calculation of the forces exerted between two cuboidal magnets," *IEEE transactions on Magnetics*, vol. 20, no. 5, pp. 192-1964, 1984.

[13] J. L. G. Janssen, J. J. H. Paulides, and E. A. Lomonova, "3D analytical field calculation using triangular magnet segments applied to a skewed linear permanent magnet actuator," *COMPEL*, vol. 29, no. 4, pp. 984–993, 2010.

M. Kleijer was born in Haarlem, The Netherlands, in 1994. He received the M.Sc. degree in electrical engineering in 2019 from the Eindhoven University of Technology, Eindhoven, The Netherlands. He is currently working towards the Ph.D. degree in the Electromechanics and Power Electronics Group of the Department of Electrical Engineering, Eindhoven University of Technology, Eindhoven, The Netherlands. His research focus is on the modeling and the design of linear and planar motors with high force densities.

J. W. Jansen received the M.Sc. degree (cum laude) in electrical engineering in 2003 and the Ph.D. degree in magnetically levitated planar actuator technology from the Eindhoven University of Technology, Eindhoven, The Netherlands. He is currently system architect in Prodrive Technologies, Son, the Netherlands, and (part time) assistant professor in the Electromechanics and Power Electronics group of the Eindhoven University of Technology. His research interests include magnetic levitation and the analysis and design of linear and planar actuators.

E. A. Lomonova was born in Moscow, Russia. She received the M.Sc. (cum laude) and Ph.D. (cum laude) degrees in electromechanical engineering from the Moscow State Aviation Institute (TU), Moscow, in 1982 and 1993, respectively. She is currently a Full professor and Chair of the Electromechanics and Power Electronics group at the Eindhoven University of Technology, Eindhoven, The Netherlands. She has worked on electromechanical actuator design and optimization and development of advanced mechatronics systems.